J Biol Inorg Chem (2009) 14:35–49
DOI 10.1007/s00775-008-0422-3

ORIGINAL PAPER

Comparative Fe and Zn K-edge X-ray absorption spectroscopic study of the ferroxidase centres of human H-chain ferritin and bacterioferritin from *Desulfovibrio desulfuricans*

L. Toussaint · M. G. Cuypers · L. Bertrand · L. Hue · C. V. Romão · L. M. Saraiva · M. Teixeira · W. Meyer-Klaucke · M. C. Feiters · R. R. Crichton

Received: 11 January 2008 / Accepted: 12 August 2008 / Published online: 3 September 2008

Abstract Iron uptake by the ubiquitous iron-storage protein ferritin involves the oxidation of two Fe(II) ions located at the highly conserved dinuclear "ferroxidase centre" in individual subunits. We have measured X-ray absorption spectra of four mutants (K86Q, K86Q/E27D, K86Q/E107D, and K86Q/E27D/E107D, involving variations of Glu to Asp on either or both sides of the dinuclear ferroxidase site) of recombinant human H-chain ferritin (rHuHF) in their complexes with reactive Fe(II) and redox-inactive Zn(II). The results for Fe–rHuHf are compared with those for recombinant *Desulfovibrio desulfuricans* bacterioferritin (DdBfr) in three states: oxidised, reduced, and oxidised/Chelex®-treated. The X-ray absorption near-edge region of the spectrum allows the oxidation state of the iron ions to be assessed. Extended X-ray absorption fine structure simulations have yielded accurate geometric information that represents an important refinement of the crystal structure of DdBfr; most metal–ligand bonds are shortened and there is a decrease in ionic radius going from the Fe(II) to the Fe(III) state. The Chelex®-treated sample is found to be partly mineralised, giving an indication of the state of iron in the cycled-oxidised (reduced, then

L. Toussaint and M. G. Cuypers contributed equally to this work.

Electronic supplementary material The online version of this article (doi:10.1007/s00775-008-0422-3) contains supplementary material, which is available to authorized users.

L. Toussaint · R. R. Crichton (✉)
Unité de Biochimie, Institut des Sciences de la Vie,
Université Catholique de Louvain,
Croix du Sud, 4-5, boite 3,
1348 Louvain-la-Neuve, Belgium
e-mail: crichton@bioc.ucl.ac.be

M. G. Cuypers
Macromolecular Crystallography Group, ESRF,
BP-220, 38043 Grenoble Cedex, France

L. Bertrand · L. Hue
Unité Hormones et Métabolisme,
Université Catholique de Louvain, UCL 75-29,
Avenue Hippocrate 75, 1200 Brussels, Belgium

L. Bertrand
Division of Cardiology,
Université Catholique de Louvain, UCL 53-49,
Avenue E. Mounier 52,
1200 Brussels, Belgium

C. V. Romão · L. M. Saraiva · M. Teixeira
Instituto de Tecnologia Química e Biológica,
Universidade Nova de Lisboa,
Av. República, EAN, Apartado 127,
2781-901 Oeiras, Portugal

W. Meyer-Klaucke
EMBL,
Outstation Hamburg, Notkestrasse 85,
22603 Hamburg, Germany

M. C. Feiters (✉)
Department of Organic Chemistry,
Institute for Molecules and Materials,
Radboud University Nijmegen,
135 Heyendaalseweg, 6525 AJ Nijmegen,
The Netherlands
e-mail: m.feiters@science.ru.nl

oxidised) form of DdBfr, where the crystal structure shows the dinuclear site to be only half occupied. In the case of rHuHF the complexes with Zn(II) reveal a surprising similarity between the variants, indicating that the rHuHf dinuclear site is rigid. In spite of this, the rHuHf complexes with Fe(II) show a variation in reactivity that is reflected in the iron oxidation states and coordination geometries.

Keywords Ferritin · Iron-storage protein · Non-haem iron · Diiron ferroxidase centre · Zinc-substituted protein

Abbreviations

BVSA	Bond valence sum analysis
CSD	Cambridge Structural Database
DdBfr	Bacterioferritin from *Desulfovibrio desulfuricans*
EMBL	European Molecular Biology Laboratory
EXAFS	Extended X-ray absorption fine structure
HuHF	Human H-chain ferritin
Mes	2-Morpholinoethanesulphonic acid
rHuHF	Recombinant human H-chain ferritin
Tris–HCl	Tris(hydroxymethyl)aminomethane hydrochloride
XANES	X-ray absorption near-edge structure
XAS	X-ray absorption spectroscopy

Introduction

Ferritins are ubiquitous proteins that concentrate, store, and detoxify intracellular iron. They do this by catalysing the oxidation of Fe(II) at dinuclear ferroxidase centres: the Fe(III) then migrates to nucleation sites within the internal protein cavity, where it is deposited as an inorganic mineral phase. Ferritins are widespread in nature, being found in bacteria and archaea as well as in eukaryotes. Their molecules are mostly assemblies of 24 structurally equivalent subunits related by octahedral 432 symmetry which form a nearly spherical shell of approximately 480 kDa with an 80-Å-diameter iron-storage cavity in which up to 4,500 iron ions can be accumulated. The protein subunits are folded in compact, four-helix bundles [1].

Most vertebrate ferritins are formed from two different subunits, H and L, although amphibians have a third subunit, M. The conserved residues essential for the ferroxidase activity, Glu27, Tyr34, Glu61, Glu62, His65, Glu107, and Gln141 (human H-chain numbering) are found only in H-type ferritins [2–4]. Crystal structures of the metal centre in recombinant (K86Q, for ease of crystallisation) human H-chain ferritin (rHuHF) [5] and in *Escherichia coli* [6] have been reported (see Fig. 1a for a schematic representation of

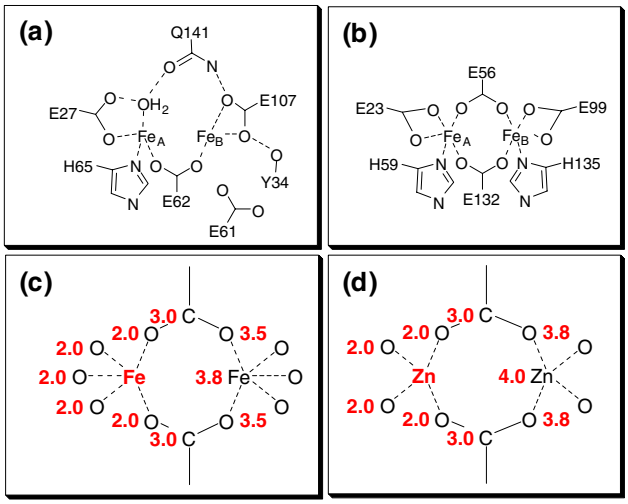

Fig. 1 The ferroxidase site. **a** Human H-chain ferritin, adapted from [8] (*E61* is conserved and was implied in metal coordination in early crystallographic studies [5, 6]). **b** Oxidised *Desulfovibrio desulfuricans* bacterioferritin, adapted from [9] structure *A* (*E99* is asymmetric bidentate in the reduced structure *B*, and monodentate in the aerobically crystallised/cycled-oxidised structure *C*). **c**, **d** Starting models for the extended X-ray absorption fine structure simulations of iron- and zinc-loaded ferritins, respectively, with the *numbers in red* indicating the distance to the metal atom in *red*

the protein ligands). The diiron centres in animal H ferritins are relatively labile and the iron can move from the dinuclear site into the iron-storage cavity upon oxidation, in line with the aforementioned mechanism of uptake as Fe(II) and storage as Fe(III). To avoid this, Zn(II) has been used as a redox-stable alternative to Fe(II) [7] and recently some of us reported crystal structures of the zinc derivatives of rHuHF and some other variants [8].

Bacterioferritins differ from mammalian-type ferritins in terms of amino acid sequence, immunological cross reactivity, composition of the iron core, and particularly the presence of one haem group per subunit dimer. The bacterioferritin from the anaerobic sulphate/nitrate reducer *Desulfovibrio desulfuricans* (DdBfr) has in its native form a fully occupied diiron ferroxidase centre (see Fig. 1b for a schematic representation), but without a central ferrihydrite core. When isolated from the bacterium under anaerobic conditions it has a total of 60 iron atoms per protein molecule, consisting of 24 diiron centres and 12 haem irons, as shown in the crystal structure [9]. However, although iron in DdBfr is found in the diiron centre, in principle a larger amount of iron can be stored inside the cavity of the protein.

With its large core full of iron, ferritin was an obvious target for early biological extended X-ray absorption fine structure (EXAFS) studies [10]. More ambitious studies in which apoferritin was reconstituted with just enough iron to fill the dinuclear ferroxidase site, resulting in samples much more dilute in iron, followed later [11]. EXAFS was also used to compare the ferritin core with accurate synthetic

models [12]. In a recent stopped-flow EXAFS study on the human H-chain ferritin (HuHF) ferroxidase site, evidence was presented for intermediates with Fe–Fe distances as short as 2.5 Å in the reaction of the bisiron(II) site with oxygen [13]. To evaluate the importance of the distance between the iron ions in the ferroxidase centre in rHuHF for the reactivity, we have constructed HuHF site-directed mutants in which the Glu residues on either side of the dinuclear iron site, Glu107 or Glu27, alone or together, are substituted by Asp. All human ferritin proteins studied in this work contained the Lys86 to Gln substitution to allow crystallisation [5]; for convenience the reference protein rHuHF-K86Q is referred to as the "wild-type" rHuHF, and the other mutants, in which one or more Glu residues have been mutated in addition to the K86Q mutation, are named rHuHF-E107D, rHuHF-E27D, and rHuHF-E107D/E27D. We have recently reported the crystal structures of the recombinant apoproteins and zinc complexes [8]. In the present study, the iron in the ferroxidase sites of these rHuHF mutants and the zinc in their Zn(II) derivatives are compared with the iron in the relatively stable dinuclear ferroxidase site in DdBfr by XAS. The DdBfr used in this EXAFS study is not the wild-type DdBfr studied by crystallography [9], but a recombinant produced in *E. coli* into which the diiron (ferroxidase) centre has been reconstituted with iron and the haem cofactor is absent. The zinc EXAFS results show that the rHuHF mutants are remarkably similar in structure, but the iron EXAFS reveals differences in reactivity. The DdBfr results show that the iron–ligand distances are shorter than in the crystallographic study, that the iron ion in the reduced state has an ionic radius which is significantly larger than that in the other states, in line with reduction from Fe(III) to Fe(II), and that the iron in an iron-containing protein sample that has been exposed to air is at least partly mineralised.

Materials and methods

Cloning, overexpression, and purification of DdBfr

For expression purposes, homologous oligonucleotides that allowed the introduction in the *Bfr* gene of an *Nde*I restriction site, at the start codon, and a *Bam*HI restriction site, downstream of the stop codon, were designed. By means of a PCR, using the oligonucleotides, *Pfu* polymerase (Stratagene) and pUBfRd plasmid [14], we achieved amplification of the complete *Bfr* gene (540 bp). After purification, the 540-bp fragment of *Bfr* was cloned in pT7-7, previously cut with the appropriated restriction enzymes, and transformed in *E. coli* $DH_{5\alpha}$ cells [15]. The resultant recombinant plasmid, pT7Bfr, was isolated and sequenced and ensured the integrity of the gene.

Cells of *E. coli* BL_{21}-Gold (DE_3) (Promega) freshly transformed with pT7Bfr were grown overnight, at 310 K, in Luria–Bertani medium with ampicillin (100 μg/mL) under aerobic conditions. This overnight culture was used (1%) to inoculate fresh Luria–Bertani media and when the cells reached a cell density corresponding to an optical density at 600 nm of 0.8, 400 μM isopropyl-thio-β-D-galactoside was added. After 4 h, cells were harvested by centrifugation and resuspended into 10 mM tris(hydroxymethyl)aminomethane hydrochloride (Tris–HCl), pH 7.5, and broken in a French pressure cell (SLM; Aminco) at 9,000 psi. Analysis of the recombinant cells revealed that the overproduced DdBfr protein was present in inclusion bodies. Hence, inclusion bodies were collected by a low-speed centrifugation (5,000*g* for 10 min). The pellet was dissolved in 20 mM Tris–HCl pH 7.6 (buffer A) which contained 8 M urea, 0.5 M NaCl, and 5 mM dithiotreitol and the mixture was stirred for 30 min, at room temperature. The insoluble material was then removed by a centrifugation step performed at 17,000*g* for 15 min. For reconstitution purposes, the supernatant that was collected by centrifugation was then dialysed in consecutive steps by successive additions of fresh buffer. To this end, after an initial 6-h dialysis in 1 L of 8 M urea, the protein suspension was dialysed eight times, in time intervals of 6 h, in 250 mL of buffer A. A final dialysis in 2 L of buffer A plus 150 mM NaCl was performed over 12 h. The solution was centrifuged at 5,000*g* for 20 min and the supernatant was concentrated in a diaflow apparatus with a YM3 membrane (Amicon). The sample was again centrifuged, at 11,600*g* for 30 min, and was then applied onto a Superdex column, S-75 (XK26/53), using buffer A plus 150 mM NaCl with a flow of 0.75 mL/min. After this purification step, the protein, identified by western blotting with antibodies raised against the native Dd haemoferritin, was found to be pure in sodium dodecyl sulphate polyacrylamide gel electrophoresis. The recombinant DdBfr was isolated in apoform, i.e., with no haem or iron content.

Bacterioferritin metal loading

The protein was concentrated and diluted in 0.1 M 2-morpholinoethanesulphonic acid (Mes) pH 7.0 with 0.2 M NaCl buffer three times to remove Tris–HCl from the sample. The water solution used to dissolve $(NH_4)_2Fe(SO_4)_2$ was degassed under vacuum for 30 min and flushed with argon for 30 min. The oxygen-free iron stock solution was added to DdBfr to yield a final concentration of 36.5 mg/mL of 2.1 irons by protein monomer. The iron-loaded sample was left for 1 h in an anaerobic environment before it was frozen in the sample holder (reduced DdBfr sample). This reduced iron-loaded DdBfr sample was recycled after beam exposure and allowed to oxidise under an air atmosphere for 1 h at room temperature. The oxidised sample was then loaded

on the sample holder and frozen for analysis (oxidised DdBfr sample).

A distinct sample was treated for excess iron removal with a Chelex® resin following iron loading. The DdBfr was loaded with 2.1 irons per protein monomer in 0.1 M Mes buffer at pH 6.5. It was then left for oxidation for 1 h before being filtered slowly with Chelex® resin squeezed into a small syringe. The diluted iron-loaded protein gathered was concentrated to 20.5 mg/mL (oxidised/Chelex®-treated DdBfr sample). Iron determination analysis by inductively coupled plasma revealed that the freshly purified recombinant protein was metal-free and each subunit of the Chelex®-treated sample contained 1.35 irons per protein subunit.

Human ferritin recombinants

The complete HuHF ferritin complementary DNA was introduced into pAS expression plasmid [16, 17]. The ferritin-encoding DNA region was amplified by PCR containing oligonucleotide primers containing base changes necessary to produce the required mutations: Glu107-Asp, or Glu27-Asp, or both. The PCR product was subcloned into the pGEM-T vector using the 3′-T overhangs. The resulting plasmid was electroporated in TG1 and sequenced. Finally the EcoRV-SphI fragment containing the required mutations was reinserted into expression plasmid. Production and purification of recombinant apoferritins are described elsewhere [16].

HuHf metal loading

The metal to protein subunit ratio was fixed to 2, to saturate the ferroxidase centre and avoid metal complexation in other weaker metal-binding sites. For iron-loaded protein, all solutions were degassed for 30 min with argon bubbling except the protein to avoid denaturing. Under an argon atmosphere, 5 μL of 0.381 M iron solution (pH 2, ratio 2:1 per subunit) was added to 1 mL of 20 mg/mL protein solution (i.e. 3.96×10^{-5} M protein, 25 mM degassed Mes buffer, pH 6.5). Then 10% Chelex® was added to the reaction tube and mixed thoroughly, and the mixture was filtered through a 4.5-μm Millipore unit. The samples were allowed to oxidise under an ambient atmosphere for 10 min. For zinc-loaded ferritins, 500 μL zinc solution (2.86 mM $ZnCl_2$) was added to 25 mL protein solution (1.6 mg/mL 0.05 M Mes, pH 6.5). The resulting solution was dialysed against 0.05 M Mes, pH 6.5 and concentrated to 500 μL (final protein concentration 40 mg/mL).

X-ray absorption spectroscopy sample preparation

The X-ray absorption spectroscopy (XAS) sample cell consists of a poly(vinyl chloride) body ($29 \times 24 \times 1$ mm^3) with a rectangular aperture (15×10 mm^2), forming the sample chamber (150 μL). Two rectangular pieces (windows) of Kapton (polyimide film) (24×18 mm^2) were glued on both sides of the cell surrounding the aperture using cyanoacrylate glue (Permacol). The cell was filled with the protein samples through the radial perforations, which were subsequently sealed with a small drop of glue. The sample was then rapidly frozen in liquid nitrogen to prevent leakages, and stored in a liquid-nitrogen-filled Dewar vessel until the XAS measurement.

XAS measurements

The EXAFS measurements reported here were carried out at the EXAFS station of the European Molecular Biology Laboratory (EMBL) Outstation at the Deutsche Elektronen Synchrotron (DESY) in Hamburg, Germany. The EXAFS station features an order-sorting (Si[111] double crystal) monochromator [18], which was set at 50% of peak intensity to suppress harmonics, a CANBERRA 13-element solid-state fluorescence detector, and an energy-calibration device [19]. For fluorescence-mode measurements the detector was placed at an angle of 90° in the horizontal plane with respect to the radiation beam. The cell must be placed under an angle of 45° to the beam to allow fluorescence radiation to be collected by the detector. The EXAFS scans were acquired around the zinc K-edge (9,660 eV) between 9,350 and 10,359 eV, and the iron K-edge (7,120 eV) between 6,900 and (initially) 8,000, later 7,600 eV. Between 15 and 25 scans per sample were taken. The X-ray absorption near-edge structure (XANES) regions of the scans were compared before averaging to check for any changes in valence state and/or ligand geometry during exposure to X-rays; none were detected. It was found that some of the detectors were hit at the iron edge by X-ray diffraction peaks (in addition to the fluorescence); this is presumably due to small ice crystals, although addition of glycerol (up to 20% v/v) as a cryoprotectant failed to improve the quality of the data. As a result not all detector contributions could be included in the summation, resulting in a lower signal-to-noise ratio than for the zinc EXAFS, and the iron EXAFS had to be truncated at 475 eV ($k \approx 11$ Å^{-1}). The samples were kept at 20 K in the helium exchange gas atmosphere of a closed-cycle cryostat during the measurements. During data collection, the storage ring DORIS III was operated at 4.5 GeV in the dedicated mode with ring currents between 140 and 85 mA.

EXAFS data reduction and simulations

Data reduction was carried out with the EMBL Outstation data-reduction package [20] including the energy-

calibration programs CALIB and ROTAX, the averaging program AVERAGE, and the background-subtraction program REMOVE. Simulations of the calibrated, averaged, and background-subtracted EXAFS were carried out using default settings (von Barth ground-state energy, Hedin-Lundqvist excited-state exchange term) in the PC-compatible version (9.272) of the program EXCURVE [21, 22] for the ab initio calculation of phase-shift and back-scattering factors. As the starting point for our single scattering simulations for iron and zinc EXAFS we adopted the models of Fig. 1c and d, respectively, that were deliberately simplified and made symmetrical compared with the crystal structures. The parameters of this model (occupancy, distance, and Debye–Waller-type factor for each shell, and the threshold energy, ΔEF) were iteratively refined. The significance of each contribution to the fit was assessed from decreases in the values of the fit index and χ^2 (Table S1).

In simulations based on Brookhaven Protein Data Bank (.pdb) files, the ligand atoms within 5 Å of each iron in the ferroxidase site were taken from the relevant .pdb files [1nfv for isolated/reoxidised (A), and 1nf4 for reduced (B)] and grouped in two clusters, one around each of the iron ions Fe_A and Fe_B which were assumed to contribute equally to the EXAFS. The atoms of the amino acid side chains were grouped in units; contrary to the simulations based on the simplified model described above, the multiple scattering effects within such units were also calculated, using the default (small-atom approach [23]) settings of EXCURVE. Before refinement, the atoms for the shells in the .pdb files up to 3.4 Å were also grouped around average values, with values for the Debye–Waller-type factors that increased with distance, matching the intensity of the peak in the phase-corrected Fourier transform. Iterative refinement of the simulation was carried out with just a few parameters: ΔEF, distances for a close and a more remote subshell of the main shell, and for the shells at approximately 3.0 and 3.4 Å. Attempts to include the Debye–Waller-type factors in these refinements led to situations where these refined to lower values for shells further away from the absorber and were therefore abandoned. In view of the good agreement already existing in the simulation based on the non-adjusted .pdb file, the outer shells were not adjusted or refined.

Results and discussion

Desulfovibrio desulfuricans bacterioferritin

XANES and EXAFS

With its relatively stable ferroxidase site which has been crystallographically characterised in various states, DdBfr serves as an anchor point for this study. In contrast to the native DdBfr, which contains haem and a fully loaded diiron ferroxidase centre, the recombinant DdBfr studied in this work is obtained free of haem and iron. This recombinant DdBfr was reconstituted (see "Materials and methods" for details) with Fe(II) and oxidised to give samples corresponding to the states referred to as oxidised, reduced, and oxidised/Chelex®-treated. In the crystallographic study of native DdBfr [9], three different DdBfr structures were determined, viz., structures A (as isolated, anaerobically purified, and aerobically crystallised), B (crystal reduced with dithionite), and C (solution reduced with dithionite, cleaned by gel filtration, and anaerobically crystallised). As shown in Fig. 2, the iron XANES edge position (7,121.4 eV) of bisiron(II) DdBfr (reduced) was significantly shifted (by 1.3 to 7,222.7 eV) upon exposure to air (oxidised DdBfr), confirming the change in valence state expected for iron oxidation. Using the absolute energy calibration of the EMBL EXAFS station [19], we found that the edge energies are not subject to accidental shifts due to, for example, variations in the angle at which the X-ray beam hits the monochromator crystals; they are also

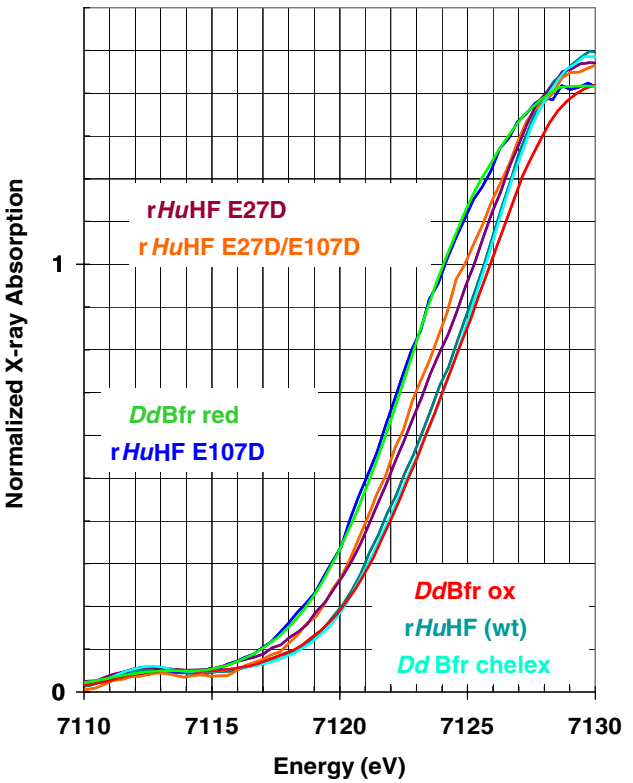

Fig. 2 Iron K-edge of iron-loaded ferritins, from low to high energy: *blue*, rHuHF-E107D (rHuHF is recombinant human H-chain ferritin); *green*, reduced bacterioferritin from *Desulfovibrio desulfuricans* (DdBfr); *orange*, rHuHF-E27D/E107D; *brown*, rHuHF-E27D; *grey*, "wild-type" rHuHF (K86Q); *turquoise*, Chelex®-treated DdBfr; *red*, oxidised DdBfr

in line with literature data on ferritin in various oxidation states [24]. No reduction of the metal ion in the metalloprotein samples by X-rays was detectable, because neither a shift in the edge position nor a lowering of the intensity of the first maximum in the X-ray absorption as a function of exposure time was observed.

It was of course of interest to see if the difference in edge position and hence in valence state was in any way reflected in the bond distances and occupancies to be derived from the EXAFS. The EXAFS is an average of contributions of the iron ions in the left and right ferroxidase sites, and even though most Fe–O/N distances are probably similar, it is only the Fe–Fe distance that is the same for both. In our initial simulations we adopted a model (Fig. 1c) that was deliberately simplified (including substitution of the single imidazole nitrogen ligand donor atom per iron, which is not resolved from the other first shell ligands, by another oxygen, which is virtually indistinguishable in EXAFS) and made symmetrical compared with the crystal structure (Fig. 1b); this model has a number of independent parameters to be refined iteratively that is as low as possible, but it does account for all the resolved shells in such a way that the results can still be related to a molecular model for the ferroxidase site. One would normally not expect to detect the non-coordinating oxygen in a carboxylate group; in the model of Fig. 1c this is more likely because of its rigidity (a ring of two carboxylate and two metal ions holding each other in place, leading to more correlated thermal motion, and hence lower values for the Debye–Waller-type factors, for all the absorber–backscatterer pairs involved) and geometry (the Fe–O–C and Fe–O–O angles are approximately 140° and 125°, respectively, which makes enhancement of the contribution of the remote atom by multiple scattering effects more likely). It has to be noted that simulations based on models such as in Fig. 1c, where atoms are not grouped in a multiple scattering unit, and only single scattering contributions are considered, might lead to relatively large errors in the outer-shell occupancies and even distances owing to the neglect of these effects. Taking this approach, simulations (Fig. 3, Table 1) using EXCURVE [21, 22] show that the average Fe–O/N ligand distance changes from 2.02 Å for the reduced sample to 1.99 Å for the oxidised sample, in line with the shorter ionic radius expected for the Fe(III) ion compared with the Fe(II) ion. The Fe–Fe distances for oxidised and reduced protein obtained from these refined simulations are much more similar than those in the crystal structure, viz. EXAFS gives 3.810 Å for reduced versus 3.882 Å for oxidised (crystallography gives 3.99 Å for structure A vs. 3.71 Å for structure). It should be noted, however, that the effect of inclusion of the Fe–Fe contribution on the fit index is small (Table S1), and that satisfactory refined simulations with fit indices only marginally higher than those for the simulations that are shown here can be obtained when the iron and remote oxygen shells are interchanged, resulting in Fe–Fe distances of approximately 3.4 Å, which is significantly shorter than the crystallographic values. Such a model for the simulations of the ferroxidase EXAFS would be more difficult to link with either of models b and c in Fig. 1, however. There are examples of high-resolution small-molecule crystal structures that feature Fe–Fe distances similar to the ones found in the DdBfr crystal structure and in our final EXAFS simulations, such as that of

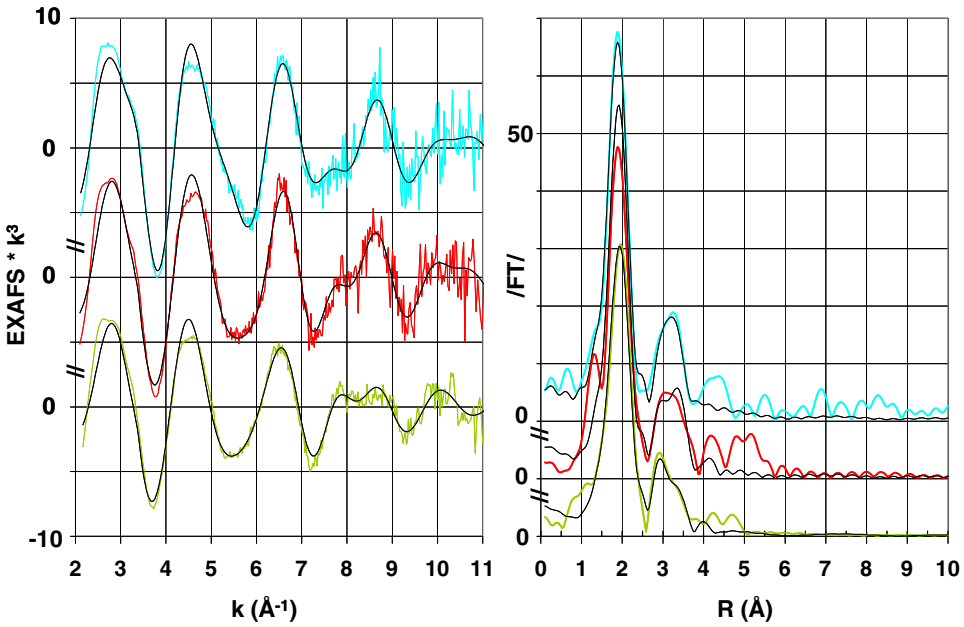

Fig. 3 k^3-weighted iron K extended X-ray absorption fine structure (EXAFS) (*left panel*) and corresponding phase-corrected Fourier transform (*right*) of DdBfr. Coloured traces, experimental: *turquoise*, Chelex®-treated; *red*, oxidised; *green*, reduced; *black traces*, corresponding simulations with the parameters listed in Table 1

Table 1 Refined parameters for the iron K extended X-ray absorption fine structure (EXAFS) simulations shown in Fig. 3

	Oxidised	Reduced	Chelex®-treated
Shell: O	5.2 at 1.99 (0.017)	4.9 at 2.02 (0.022)	5.2 at 1.97 (0.018)
σ first shell (Å)	0.09	0.10	0.09
Shell: C	2.0 at 3.02 (0.003)	2.1 at 3.01 (0.003)	2.7 at 3.05 (0.007)
Shell: O	2.6 at 3.39 (0.004)	2.2 at 3.39 (0.013)	7.9 at 3.49 (0.030)
Shell: Fe	1.1 at 3.88 (0.030)	0.6 at 3.81 (0.025)	1.5 at 3.40 (0.020)
ΔEF	−4.1144	−3.0322	−3.7810
Energy range (eV)	2.5–475	2.5–475	3–475
Fit index	0.1259×10^{-3}	0.1066×10^{-3}	0.1133×10^{-3}
Edge (eV)[a]	7,122.7	7,121.4	7,122.4

Distances in ångströms; Debye–Waller-type factors as $2\sigma^2$ in parentheses in square ångströms

ΔEF threshold energy

[a] Energy position at half height

(μ_2-acetato)-(μ_2-*m*-xylylenediamine bis(Kemp's triacid) imido)-bis(*N*-methylimidazol-3-yl)-tris(methanol)-diiron (II) tetrafluoroborate (Cambridge Structural Database, CSD, code REKFUI, Fe–Fe distance 3.827 Å) [25].

For the oxidised/Chelex®-treated DdBfr sample the situation is different: an even shorter average iron–ligand distance (1.97 Å, compatible with five-coordination to six-coordination according to bond valence sum analysis, BVSA, as discussed later) is observed, along with an unambiguous Fe–Fe contribution (Table S1), with increased (1.5) occupancy, at 3.39 Å. The crystal structure of the wild-type DdBfr that was aerobically crystallised (structure C, the cycled-oxidised, or reduced then oxidised structure) shows that only one of the iron sites in the ferroxidase site, the Fe_B (right) site, is occupied, in which case no Fe–Fe distance is expected to be detectable by EXAFS. The distance of 3.4 Å is more characteristic of mineralisation of iron together with oxygen in the ferritin core; compare this with the results for fully loaded horse spleen ferritin [12] (six oxygens at 1.96 Å, 1.1 irons at 3.43 Å), and the spectra resemble those reported in [26] which were simulated with five oxygens at 1.95 Å and two iron contributions (3.7 at 3.00 Å, and 2.0 at 3.53 Å). A distance of 3.38 Å for a Fe–Fe contribution, along with five to six nitrogens/oxygens at 1.96 Å, has also been observed for horse spleen apoferritin reconstituted with two Fe(III) per subunit [11], and most likely represents a protein-bound polynuclear Fe–O cluster there. The EXAFS result for oxidised/Chelex®-treated DdBfr, including the increased occupancies of the remote oxygen and iron shells, points to the presence of biomineralised iron in the sample. This implies that following oxidation part of the iron leaks from the ferroxidase site, leaving only the Fe_B site occupied, and forms Fe–O clusters so small and so irregular that they escaped detection in the crystallographic study of the wild type [9]. Clearly, of the three states of DdBfr studied here, the oxidised/Chelex®-treated sample is least interesting in terms of direct comparison of EXAFS and crystallography results, but the EXAFS does give an indication of where the iron supposed to be present in the Fe_A site in structure C of the crystallographic study may have gone.

Comparison with the crystal structure

The crystal structures of the as-isolated (A) and reduced (B) wild-type DdBfr [9] show little symmetry in the iron coordination (Table 2), and no indication of a difference in ionic radius between the Fe(II) and Fe(III) states. It is of interest to compare the EXAFS results for the oxidised and reduced DdBfr samples with what are most likely to be their crystallographic analogues, the as-isolated structure A and the reduced structure B, respectively. The average ligand distance determined by EXAFS (Table 1) for oxidised DdBfr is shorter by 0.25 Å and that for reduced DdBfr is shorter by 0.21 Å. The difference in the average ligand distances is larger than can be explained by the accepted errors for either technique (±0.02 Å for EXAFS, ±0.14 Å for crystallography). From the crystallographic data for the DdBfr ferroxidase site, the static disorder σ_{static} can be calculated on the basis of the deviations of the iron–ligand distances from the average value (Table 2), giving values of 0.15 Å for the as-isolated form A, and 0.14 Å for the reduced form B. The Debye–Waller-type factor σ (or EXAFS Debye–Waller factor, refined as $2\sigma^2$ in EXCURVE simulations) is the sum of the contributions representing static (σ_{static}) and thermal ($\sigma_{thermal}$) disorder and can therefore be considered to indicate the maximum possible static disorder or variance, assuming that there is no thermal disorder at 20 K. The Debye–Waller-type factors refine to 0.09 and 0.10 Å for oxidised and reduced forms, respectively. These values are significantly lower than the

Table 2 Comparison of iron–ligand distances (Å) determined by crystallography (normal, adapted from [9], see Fig. 1b for a schematic representation) and adjusted/refined by EXAFS (*italic*)

	Protein Data Bank code					
	1nfv		1nf4		1nf6	
	(A) as isolated[a]		(B) reduced[b]		(C) cycled-oxidised[c]	
	Fe_A	Fe_B	Fe_A	Fe_B	Fe_A	Fe_B
Glu23	2.24, 2.24 *2.08*, *2.08*	–	2.26, 2.26 *2.09*, *2.09*	–	–	–
Glu56	2.12, *1.94*	2.16, *1.94*	2.09, *1.94*	2.14, *1.94*	–	2.97, 2.06 *2.97*, *1.93*
Glu99	–	2.11, 2.52 *2.08*, *2.08*	–	2.19, 2.46 *2.09*, *2.09*	–	3.07, 2.24 *3.07*, *2.01*
His135	–	2.57, *2.08*	–	2.27, *2.09*	–	2.14, *2.01*
Glu132	2.04, *1.94*	2.02, *1.94*	2.05, *1.94*	2.04, *1.94*	–	3.16, 1.93 *3.24*, *1.93*
His59	2.23, *2.08*	–	2.23, *2.09*	–	–	–
OW	–	–	2.46, *2.09*	–	–	3.63, *3.49*
Fe–Fe	3.71, *3.41*	–	3.99, *4.04*	–	–	–
Average/site	10.87/5 = 2.174 *2.02*	11.48/5 = 2.296 *2.02*	13.35/6 = 2.225 *2.04*	11.1/5 = 2.220 *2.03*	15.43/7 = 2.204	8.37/4 = 2.093 (4) *1.97*
σ	0.06	0.20	0.13	0.09	(7) 0.57	(4) 0.11
Average/σ	22.35/10 = 2.235 *2.02*	0.15	24.45/11 = 2.223 *2.04*	0.14	–	–

[a] EXAFS parameters for oxidised DdBfr; see Fig. S1a, trace iii

[b] EXAFS parameters for reduced bacterioferritin from *Desulfovibrio desulfuricans* (DdBfr); see Fig. 4 (and Fig. S1b), trace iii, and Fig. 5b

[c] EXAFS parameters for Chelex®-treated DdBfr; see. Fig. S1c, trace iii

crystallographically derived σ_{static}, which is a strong indication that the ferroxidase site is probably more symmetrical, with less spread in the iron–ligand distances, than the crystallographic model suggests. The case is comparable, albeit more complicated, to that of an early biological EXAFS study on rubredoxin, where the possibility that rubredoxin had both relatively long and short Fe–S distances was rejected [27, 28].

The longer average distance for the crystal structure is caused in part by the inclusion of both oxygens of bidentate Glu residues, and it is possible that the more remote oxygen does not contribute to the EXAFS. In the initial EXAFS simulations, the occupancy of the main shell (coordination number) refines to values around 5, but because of their strong correlation with the Debye–Waller-type factor, the error of the coordination numbers can be as high as 30%; a refined value of 5 could therefore still be 4 or 6 in reality. BVSA [29] offers an approach to use the accurate determination of bond lengths to get information about the coordination numbers. For the application to ferritin, we have neglected the contribution of the single His nitrogen per iron site and substituted it by another oxygen, keeping in mind that a typical Fe–N distance is longer than an Fe–O distance by 0.07 Å for Fe(II) and 0.1 Å for Fe(III). For the Fe(II) (reduced) protein the average Fe(II)–O ligand distance of 2.02 Å found by EXAFS is in-between those characteristic of four-coordination (1.99 Å) and five-coordination (2.07 Å). This could point to the presence of one four-coordinated and one five-coordinated site, which would imply that the longest iron–ligand contacts found in crystallographic structure B (reduced), viz. the water oxygen in the left (Fe_A) site and the remote Glu99 carboxylate oxygen in the right (Fe_B) site, both at 2.46 Å, do not contribute to the EXAFS. For the oxidised protein, the average Fe(III)–O ligand distance of 1.99 Å found by EXAFS is in-between those characteristic of five-coordination (1.95 Å) and six-coordination (2.02 Å). This means that all the ligands found in oxidised crystallographic structure A (as-isolated) probably contribute to the EXAFS, even the remote Glu99 carboxylate oxygen and His135 nitrogen found at 2.52 and 2.57 Å, respectively. There is also the possibility that coordination positions that are apparently empty in the crystal structure are taken up by small ligands, such as water, molecular oxygen, or peroxide, at a relatively short distance, that have gone undetected in the crystal structure. For the as-isolated

(oxidised) DdBfr (A) this should certainly be considered, as there is some electron density on the site of the Fe(III) corresponding to the top in Fig. 1b, which can be fitted with water and/or (per)oxo bridges, but not unequivocally, presumably because of the presence of a mixture of states. Recently [30] as-isolated DdBfr has been reinvestigated by crystallography under circumstances where radiation damage is minimised, and an end-on peroxo ligand to Fe_B could be tentatively identified. It is worth noting that such a non-protein ligand would be compatible with the occupancy determined for oxidised DdBfr by EXAFS, as well as with further considerations on the coordination number based on BVSA.

We find that the EXAFS ligand distances are in good agreement with what is expected for five- or six-coordination according to BVSA [29], especially for the Fe(III) valence state. Moreover, the crystallographic distances are much greater than those considered typical for iron on the basis of a survey of high-resolution crystal structures [31], which are 2.01 Å for Fe–O(carboxylate) and 2.08 Å for Fe–N(His). These conclusions inspire confidence in the EXAFS results. We decided to use the EXAFS simulation program EXCURVE to simulate EXAFS on the basis of crystallographic coordinates as available from the Brookhaven Protein Data Bank, a so-called .pdb file, to see where the main deviations were and by which adjustments better agreement between EXAFS and crystallography results might be reached. In these simulations, the ligand atoms within 5 Å of each iron in the ferroxidase site were taken from the relevant .pdb files [1nfv for as-isolated (A) and 1nf4 for reduced (B), applied to the oxidised and reduced DdBfr EXAFS results, respectively] and grouped in two clusters, one around each of the iron ions Fe_A and Fe_B which were assumed to contribute equally to the EXAFS. The atoms of the amino acid side chains were grouped in units; in contract to the simulations based on the simplified model described above, multiple scattering effects within such units were also calculated.

As expected after our simulations based on the symmetrised model in Fig. 1c, the initial agreement between the experimental EXAFS and the simulation based on the coordinates from the Protein Data Bank was very poor (see trace i in Fig. 4 for reduced DdBfr, and Fig. S1). Not only were the iron–ligand distances overestimated, but in addition the static disorder or variance in the iron–ligand distances was larger than expected. On the other hand, the agreement between theory and experiment for the outer shells was already very good, considering that all Debye–Waller-type factors had been arbitrarily set to 0.010 $Å^2$, and a value for ΔEF had been chosen, not refined. The agreement for the main shells was improved considerably by setting the average iron–ligand distance of this shell to the value arrived at in the preliminary simulations presented in Fig. 3 and Table 1, and adjusting the Debye–Waller-type factor for this shell by hand. Obviously this still resulted in poor agreement with the crystallographic distances, as discussed above (average crystallographic distance underestimated by 0.21–0.25 Å). It was noted that the values for the Debye–Waller-type factors used in the simulation for the first shell (0.017 $Å^2$ for oxidised, 0.022 $Å^2$ for reduced) were much higher than the value of 0.010 $Å^2$ that was arbitrarily chosen for the outer shells and found to give good agreement there. This is an artificial situation as the values for the Debye–Waller-type values are supposed to go up with the distance to the central absorber, not down. It was therefore decided to

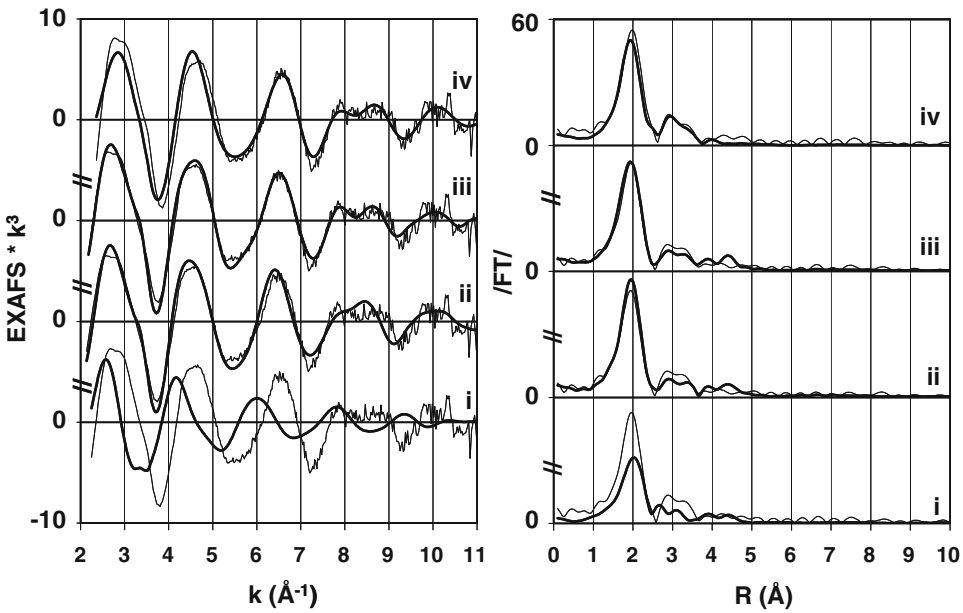

Fig. 4 k^3-weighted EXAFS (*left*) and corresponding phase-corrected Fourier transform (*right*) of reduced DdBfr. *i* EXAFS simulation on the basis of the .pdb file related to the crystal structure of reduced wild-type DdBfr [9], 1nf4 (distances in Table 2); *ii* major shells adjusted to the average EXAFS value found in the initial simulation given in trace *iv*, Fig. 3, and Table 1; *iii* simulation obtained by iterative refinement of the threshold energy and distance values, starting from the adjustment in *ii*, resulting in the distances given in italic in Table 2; *iv* simulation based on the simplified model in Fig. 1c, refining to the parameters in Table 1

split the main shell into two subshells with lower values for the Debye–Waller-type factors. Detailed inspection of the distances in Table 2 revealed that the oxygens of the bridging Glu ligands were found at relatively short distances (2.02–2.16 Å, compared with the average of 2.23 Å) from the iron ions in the crystallographic study. These (two per iron) were selected to be at relatively short distances (1.96 Å for oxidised, 1.99 Å for reduced), whereas the others were put at larger distances (2.02 Å for oxidised, 2.05 Å for reduced), in such a way that the resulting average ligand distance was close to that obtained from the EXAFS simulations based on a simplified model (Table 1; see "Materials and methods" for more details). These adjustments resulted in a significant improvement of the agreement between simulated and experimental EXAFS as can be seen from traces ii in Fig. 4 (and Fig. S1). The agreement could be even further improved by iterative refinement of the ΔEF and distance parameters (not the Debye–Waller-type factors), resulting in the satisfactory fits of traces iii in Fig. 4 (and Fig. S1). It can be seen from a comparison of the EXAFS parameters obtained in this way, given in *italic* in Table 2, that the distances to the bridging Glu oxygens need to be shortened by only approximately 0.1 Å, and to the other atoms, except the *very* remote ones, by only 0.15 Å to get agreement. This is a far less drastic shift than the 0.2–0.25-Å difference in the average values and one that is almost within the accepted error for the crystallographic distances. The adjusted distances resulting from the EXAFS are given together with the crystallographic values in *italic* in Table 2, and a graphical representation of the adjustment for the reduced DdBfr, based on .pdb file 1nf4 [9], is given in Fig. 5. It would have been of interest to investigate whether the crystallographic data of the DdBfr crystal structure are better fitted by a model based on the metal–ligand distances obtained by EXAFS. A practical problem is the large number of protein monomers (16) comprising the asymmetric unit, which means that the coordinates of the ligands of 32 iron atoms would have to be edited before the structure could be refined again. Another problem is that at the current resolution (around 2 Å for the DdBfr structures [9]), the apparent electron density around the metal ions is disturbed by termination effects in the Fourier transformation (Fourier ripple effects, see [32] for an early discussion of the case of a dinuclear iron protein). There are examples where metalloprotein structures have been improved by EXAFS studies but they are usually based on new crystallographic data with a higher resolution (see [33] for examples).

The application of the procedure described above for the reduced and oxidised DdBfr to the sample corresponding to the Chelex®-treated DdBfr using coordinates of the structure

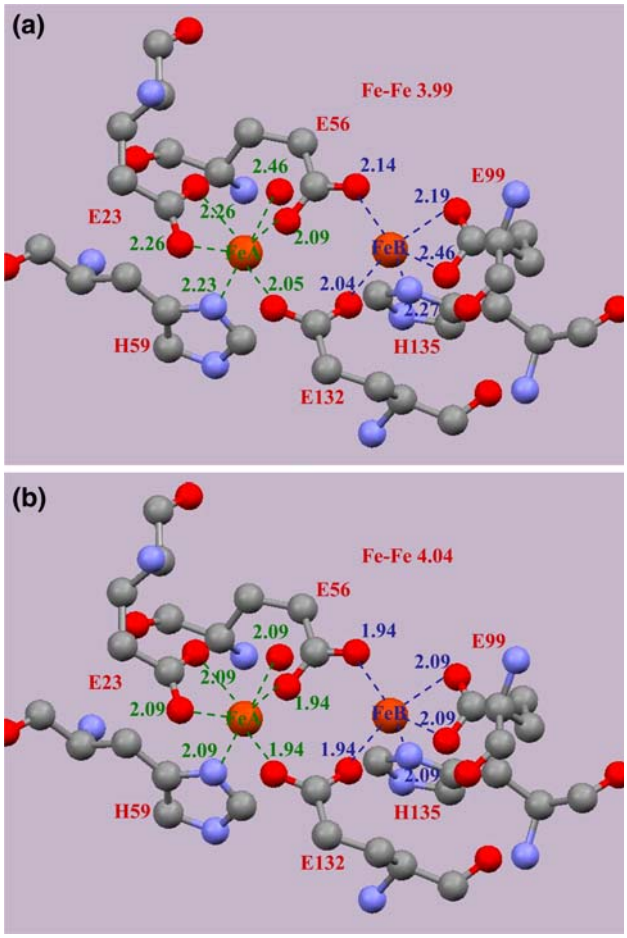

Fig. 5 Ferroxidase site in reduced DdBfr with iron–ligand distances in ångströms: **a** as determined by crystallography [9], **b** adjusted to give agreement with the EXAFS. *Grey*, carbon; *red*, oxygen; *blue*, nitrogen; *orange*, iron; hydrogens are omitted for clarity. *Green* and *blue* distance values refer to Fe_A (*left* iron ion) and Fe_B (*right*), respectively

from the crystallographic study [9] that most corresponds to it, the aerobically crystallised, cycled-oxidised (reduced, then oxidised) DdBfr (structure C, .pdb file 1nf6), was expected to be problematic. The simulations based on the simplified model (Fig. 3, Table 1) had detected the presence of a strong Fe–Fe contribution at 3.4 Å, which was not expected on the basis of the crystal structure [9], where only Fe_B is occupied. Indeed it was found necessary to add an iron contribution at 3.4 Å in the EXAFS simulation based on .pdb file 1nf6. As discussed above, this Fe–Fe distance is reminiscent of that found in polynuclear Fe–O clusters such as found in the core of ferritin loaded with iron; the simulation result confirms that at least in the EXAFS sample the iron is not only present in the ferroxidase site, but also mainly in such (bio)minerals. The fact that the EXAFS spectrum at best partially represents the Fe_B site in .pdb file 1nf6 makes it difficult to investigate the role of one or perhaps even two water ligands to this iron.

Recombinant human H-chain ferritin

Zinc-loaded rHuHF variants

A number of HuHF mutants have been studied by crystallography [8] using Zn(II) ions as redox-invariant analogues of Fe(II), and this approach to study ferritin with other metal ions such as manganese has also been taken for XAS studies [34]. The Zn K-edge spectra of the rHuHF mutants incubated with 2 M equiv of Zn(II) differs mainly in the intensity of the so-called white line, the first maximum in the X-ray absorption spectrum at 9,670 eV (white line, Fig. 6). For a coherent coordination sphere an increase in intensity in the white line can be attributed to a higher coordination number [35]. Comparing the white line intensities with those of model compounds of known coordination (Fig. 6) [36, 37], we can conclude that rHuHF-E107D and rHuHF-E107/E27D mutants, which are indistinguishable, are close to the four-coordinated model

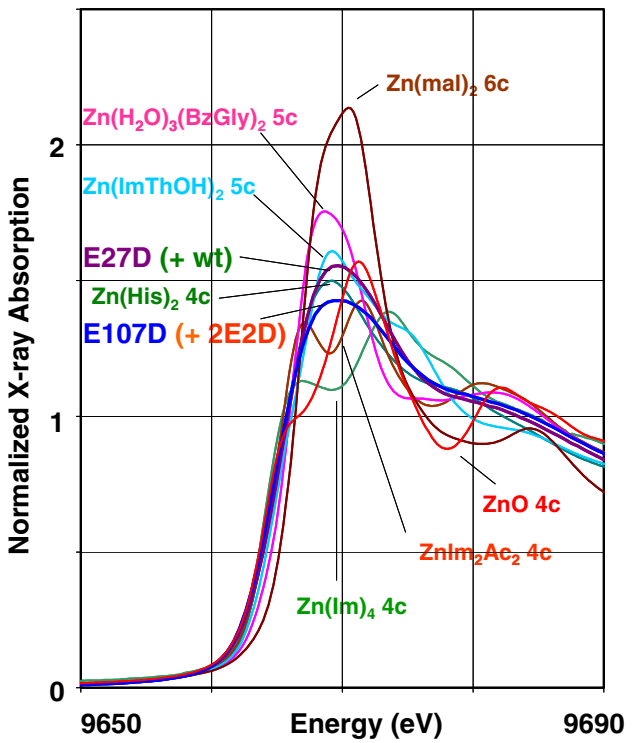

Fig. 6 Zinc K-edge of zinc-loaded rHuHF. [*Bold*: *blue*, rHuHF-E107D, colliding with *orange*: rHuHF-E27D/E107D; *violet*: r*Hu*HF-E27D, colliding with *green*: "wild-type" rHuHF (K86Q)] and zinc complexes [*thin lines*: *light green*, tetrakis(imidazole)Zn(II) diperchlorate (tetrahedral four-coordinate); *orange*, bis(acetato)bis (imidazole)Zn(II) (near tetrahedral four-coordinate); *red*, zinc oxide (tetrahedral four-coordinate); *dark green*, bis(L-histidino)Zn(II) dihydrate (tetrahedral four-coordinate); *turquoise*, bis[(imidazol-2-yl-thiophen-2-yl)methanol]zinc(II) sulphate hydrate (five-coordinate); *pink*, triaquabis(*N*-benzoylglycinato)zinc(II) dihydrate (five-coordinate); *brown*, tetraaquabis(hydrogenmaleato)zinc(II) (octahedral six-coordinate). See [36, 37] for details of the models

compounds. The intensities of the white lines of the wild type (K86Q) and the rHuHF-E27D mutant, which are also indistinguishable, are between those characteristic for four- and five-coordination, possibly indicating the presence of one four-coordinate and one five-coordinate site.

By analogy to the model for the bacterioferritin ferroxidase site (see above; Fig. 1c), a symmetrised model was constructed for the dinuclear zinc-loaded HuHF ferroxidase site (Fig. 1d). In one aspect this model is a larger simplification compared with the structure known to exist in the protein crystal structure, viz. HuHF contains only one Glu bridge (Fig. 1a), whereas bacterioferritin (Fig. 1b) and the model (Fig. 1d) contain two Glu bridges. On the other hand, the simplification of the substitution of the imidazole by another oxygen is more justified, since bacterioferritin contains two His ligands (one His ligand per metal), whereas HuHF has only one (to Fe_A). Simulations of the zinc rHuHF EXAFS spectra (Fig. 7, Table 3) reveal strong similarities. The spectra show Zn–O (probably carboxylate oxygen) contributions around 2 Å, Zn–C distances (again carboxylate) at 3 Å, and Zn–Zn distances at 4 Å. The observed Zn–Zn distances are a little shorter than the expected distances of remote imidazole ring atoms (4.2 Å). However, attempts to simulate the spectrum with rigid imidazoles failed because a remote ring atom at 4.0 Å would imply a ligand donor atom at 1.8 Å; this is not compatible with the data and moreover is chemically unrealistic. It must be concluded that the single imidazole per metal atom in the HuHF ferroxidase site does not contribute significantly to the EXAFS. This is somewhat unexpected, but it must be noted that examples where even three imidazole ligands to an iron atom do not give a detectable outer-shell contribution to the EXAFS have been reported [38]. The intensity of those EXAFS features has also been found to depend on the orientation of the imidazole ligand with respect to the metal-donor atom bond [36].

The first-shell distances (2.00–2.01 Å) are in good agreement with those expected for a four-coordinate Zn–O complex according to BVSA [29], viz. 2.03 Å, and with the Zn–O(carboxylate) distance of 2.04 Å found in the survey of high-resolution crystal structures [31], especially when the possible presence of one shorter Zn–N(His) (1.96 in BVSA, 2.00 Å in the survey) is taken into account. The lack of significant differences is surprising in view of the effects that might have been expected on the basis of the mutants of the Glu ligands on either site of the dinuclear site. However, it should be noted that the geometries, in particular the Zn–Zn distances, of the zinc-occupied ferroxidase sites as determined in the various mutants by crystallography [8] are also rather similar (3.32 Å for "wild-type" K86Q, 3.44 Å for E27D, and 3.38 Å for E107D) apart from rHuHF-E27D/E107D, which did not

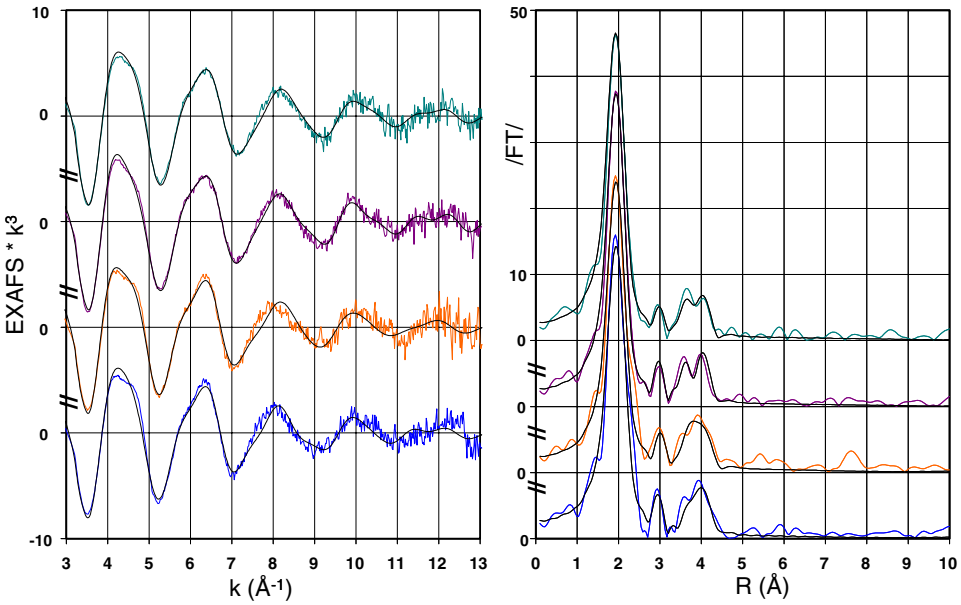

Fig. 7 k^3-weighted zinc K EXAFS (*left*) and corresponding phase-corrected Fourier transform (*right*) of rHuHF. Coloured traces, experimental: *green*, "wild-type" rHuHF (K86Q); *violet*, rHuHF-E27D; *orange*, rHuHF-E27D/E107D; *blue*, rHuHF-E107D; *black traces*, corresponding simulations with the parameters listed in Table 3

Table 3 Refined parameters for the Zn K EXAFS simulations shown in Fig. 7

	rHuHF (K86Q)	rHuHF-E27D	rHuHF-E27D/E107D	rHuHF-E107D
Shell: O	4.9 at 2.00 (0.019)	4.8 at 2.00 (0.018)	4.7 at 2.00 (0.016)	4.9 at 2.01 (0.020)
Shell: C	0.5 at 3.01 (0.004)	0.6 at 2.99 (0.001)	0.8 at 3.03 (0.006)	0.6 at 2.98 (0.001)
Shell: O	5.3 at 3.79 (0.025)	4.9 at 3.78 (0.022)	5.4 at 3.82 (0.023)	3.7 at 3.82 (0.017)
Shell: Zn	0.8 at 3.98 (0.016)	1.0 at 3.97 (0.013)	2.3 at 4.00 (0.030)	1.3 at 3.99 (0.018)
ΔEF	−10.3233	−10.3910	−11.6095	−11.9367
Energy range (eV)	25–722	25–722	25–722	25–718
Fit index	0.1059×10^{-3}	0.0901×10^{-3}	0.2297×10^{-3}	0.1588×10^{-3}

Distances in ångströms; Debye–Waller-type factors as $2\sigma^2$ in parentheses in square ångströms

rHuHF is recombinant human H-chain ferritin

have its ferroxidase site occupied with two zinc ions in the crystal structure. The Zn–Zn distances determined by crystallography [8] are much shorter than those determined by EXAFS in the present study. Additional EXAFS simulations where the zinc and oxygen shells at 4.0 and 3.8 Å are interchanged have almost as good fit indices as the ones presented in Table 3 and Fig. 7, but the Zn–Zn distance from EXAFS is under no circumstances shorter than 3.8 Å. We note that there are examples of crystal structures of synthetic dinuclear zinc complexes that feature Zn–Zn distances in this range, such as bis(μ_2-acetato)-bis(ethyl 2-cyano-3-[(2,6-di-isopropylphenyl)amino]-*N*-(2,6-diethylphenyl)prop-2-enimidoato)-dizinc (CSD code DEQTEZ, Zn–Zn distance 3.963 Å) [39] and bis((μ_2-acetato-*O*,*O*′)-(2-(2-(pyrrolidyl)ethyl)-1,3,4,5-tetramethyl-cyclopentadienyl))-dizinc (CSD code XOJSEU, Zn–Zn distance 3.823 Å) [40]. We conclude that the most important factor that determines the Zn–Zn distance is the bridging Glu (Glu62), and that moving the carboxylates of Glu27 and/or Glu107 has little effect. Crystallography shows that the zinc sites are three- or four-coordinated, with zinc–ligand distances for the "wild type" (K86Q, average 2.16 Å) and rHuHF-E27D (2.10 Å) that are longer than those determined by EXAFS, although not as long as those in the DdBfr structure. For the "wild type" and this mutant the agreement between EXAFS and crystal structure rHuHF is quite good if one moves each zinc ion 0.10–0.15 Å towards the Glu ligands at either end of the ferroxidase site, elongating the Zn–Zn distance correspondingly. For rHuHF-E107D the distance of Asp107 to the zinc ion to the right is much longer (3.2 Å) than the EXAFS distances, and probably small (water) ligands not observed in the crystal structure complete the coordination sphere for this ion. For rHuHF-E27D/E107D there is no agreement between EXAFS and crystallography, and one must conclude that the soaking of the crystals with zinc and the preparation of the zinc derivative in solution by adding 2 equiv of the metal resulted in samples with different metal loading. A more detailed comparison of the EXAFS and crystallographic results such as discussed for DdBfr is hampered by

the problem that in the rHuHF crystal structures, the Zn(II) ions have never more than three protein ligands (in one case, Zn_B in rHuHF-E107D, only one) and that only few of the non-protein ligands have been localised, whereas the EXAFS clearly indicates coordination numbers of at least four.

Iron-loaded rHuHF variants

Samples were incubated with iron under transiently anaerobic conditions under an argon atmosphere to favour the homogeneity of iron distribution; by maintaining iron in the Fe(II) form, we anticipated that, as in the case of native DdBfr [9] we would restrict iron uptake to only two iron atoms into each ferroxidase centre. Controlled oxidation was then allowed to proceed before the sample was flash-frozen and X-ray absorption data were collected on the frozen solution. In this way we expected to be able to monitor any oxidation of the iron ions, as well as their possible migration from the ferroxidase centre to the nucleation site.

The edge spectra in Fig. 2 show that the edge position of the rHuHF-E27D/E107D mutant sample is close (7,121.8 eV) to that of the reduced DdBfr (7,121.4 eV), implying that it has retained significant Fe(II) character (cf. [24]). The "wild-type" rHuHF (K86Q) edge is at 7,122.5 eV and close to that of the oxidised DdBfr, implying a significant degree of oxidation (and perhaps mineralisation). The bisiron complexes of the mutants in which only a single Glu was changed to an Asp, rHuHF-E27D and rHuHF-E107D, were found at intermediate energies. For rHuHF and rHuHF-E107D, the fast oxidation and its total absence, respectively, are in line with their observed relative reactivities in the accumulation of Fe(III) ions upon addition of Fe(II) to the apoprotein under aerobic conditions [8]. On the basis of these measurements, rHuHF-E27D was expected to be even more easily oxidised than the wild type, whereas rHuHF-E27D/E107D showed no activity at all.

Simulations of the EXAFS spectra on the basis of the symmetrised model (Fig. 1c) that was also applied to the DdBfr data were carried out to probe the environment up to 3–4 Å from the absorbing iron atom for the presence of a high-*Z* atom (iron, see Fig. 8). Some of the iron rHuHF EXAFS spectra, viz. those for rHuHF-E27D/E107D and rHuHF-E107D, have a lower signal-to-noise ratio than the others, because fewer detector contributions could be included (see "Materials and methods"); they are nevertheless included here to complement the zinc edge and EXAFS and iron edge results. The results of the best simulations are given in Table 4. Interestingly, none of the observed Fe–O distances is at 2.0 Å or higher such as observed for the zinc analogues or the iron in reduced DdBfr; all Fe–O distances fall in the range 1.97–1.99 Å, even for rHuHF-E107D, which appears to have both its irons as Fe(II) judging from the edge (Fig. 2). For this last mutant, BVSA indicates that the coordination number most likely correlated with Fe(II)–O distances of 1.99 Å is four; this means that in addition to the expected protein ligands (Glu62 for both irons, Glu27 and His65 to the left, Glu107 to the right) there is probably at least one small non-protein ligand, possibly the water oxygen already indicated for Fe_A (Fig. 1a). For the others it is between five and six, assuming considerable or complete conversion to Fe(III).

For rHuHF-E27D/E107D and rHuHF-E107D very weak Fe–Fe contributions, at respectively, 3.96 and

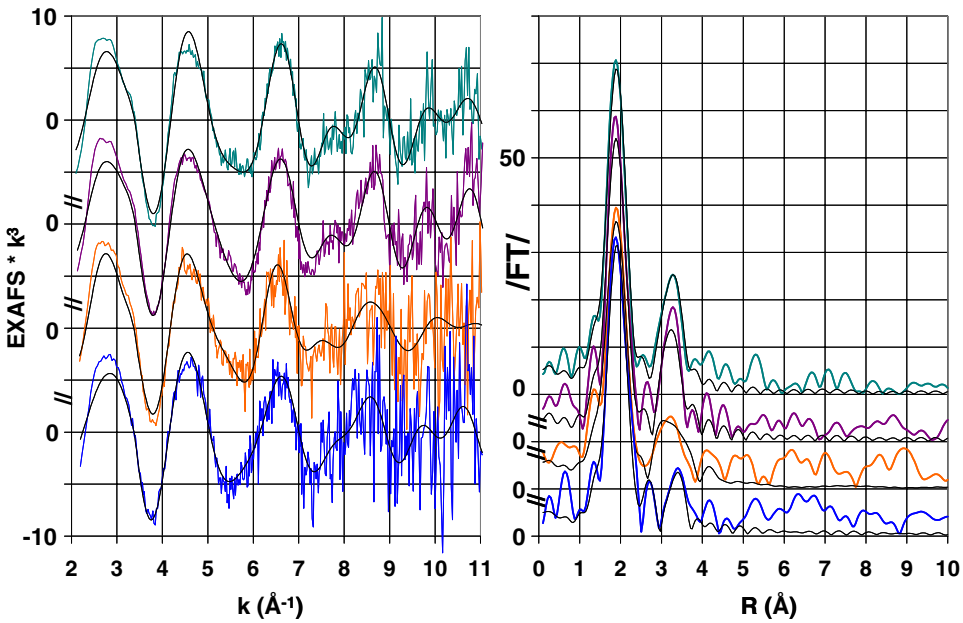

Fig. 8 k^3-weighted iron K EXAFS (*left*) and corresponding phase-corrected Fourier transform (*right*) of rHuHF. Coloured traces, experimental: *green*, "wild-type" rHuHF (K86Q); *violet*, rHuHF-E27D; *orange*, rHuHF-E27D/E107D; *blue*, rHuHF-E107D; *black traces*, corresponding simulations with the parameters listed in Table 4

Table 4 Refined parameters for the iron K EXAFS simulations shown in Fig. 8

	rHuHF (K86Q)	rHuHF- E27D	rHuHF- E27D/ E107D	rHuHF- E107D
Shell: O	5.1 at 1.98 (0.015)	4.7 at 1.97 (0.016)	5.1 at 1.98 (0.021)	4.7 at 1.99 (0.010)
Shell: C	1.2 at 3.03 (0.003)	1.7 at 3.11 (0.001)	2.7 at 3.05 (0.005)	2.7 at 2.93 (0.004)
Shell: O	4.4 at 3.49 (0.003)	4.8 at 3.55 (0.003)	6.3 at 3.46 (0.030)	3.3 at 3.32 (0.003)
Shell: Fe	1.7 at 3.38 (0.004)	2.1 at 3.40 (0.003)	1.1 at 3.96 (0.023)	1.1 at 3.12 (0.003)
ΔEF	−3.9150	−3.3515	−3.1847	−2.3904
Energy range (eV)	2.5–475	2.5–475	3–472	2.5–475
Fit index	0.1620×10^{-3}	0.2310×10^{-3}	0.4782×10^{-3}	0.6311×10^{-3}
Edge[a]	7,122.5	7,121.8	7,121.8	7,121.0

Distances in ångströms; Debye–Waller-type factors as $2\sigma^2$ in parentheses in square ångströms

[a] Energy position at half height (eV)

3.12 Å were detected, which have to be considered insignificant in view of the noise in the data; the most important conclusion from these simulations is that there are no strong Fe–Fe contributions in the 3.4-Å range. Such contributions were very strongly present in the data for rHuHF and the E27D mutant. We note that these distances are much shorter than those observed for DdBfr and zinc-loaded rHuHF but are in the same range as those found with crystallography for zinc HuHF; however, in the zinc EXAFS such short distances were not detected. Imidazole contributions were not required to simulate any of the rHuHF iron EXAFS, in line with the observations for the zinc HuHF analogues where there is also only 0.5 imidazole per metal expected. It rather looks like the presence of relatively short Fe–Fe distances for the wild type and the E27D mutant points to the presence of a significant amount of mineralised iron in those samples. This is also consistent with the relatively high occupancies of the Fe–O shells and the Fe–O distances which are a little bit too short to be all Fe–O(carboxylate) distances when compared with the distance of 2.01 Å given in the metalloprotein crystal structure survey [31]. The observation of polynuclear Fe–O cluster formation upon addition of Fe(II) ions to apoferritin is consistent with literature results [11, 41].

Concluding remarks

The X-ray absorption near-edge region of the spectrum (XANES) allows the oxidation state of the iron ions to be assessed, and reflects the oxidation state of DdBfr as well as the different reactivities of rHuHF mutants. In the case of rHuHF reconstituted with zinc, information on coordination number and geometry is derived from the XANES. Simulations of the EXAFS have yielded accurate geometric information that represents an important refinement of the crystal structure, adjusting most metal–ligand bonds to shorter distances and allowing differences between the Fe(II) and Fe(III) states that are consistent with the ionic radii to be established. Moreover, the results give a clue about the state of iron in the aerobically crystallised/cycled-oxidised form of DdBfr, where the crystal structure (C) shows the dinuclear site to be only half occupied; the EXAFS of the analogous oxidised/Chelex®-treated sample provides evidence that the other iron is used in a mineralisation process. In the case of rHuHF the complexes with the redox-inert zinc reveal a surprising similarity among the variants. This is in line with the crystal structures of three mutants, although the metal–ligand and metal–metal distances found with EXAFS are shorter and longer, respectively. The zinc results indicate that the metal–metal distances are not much affected by the mutations of Glu27 and/or Glu107 to Asp residues. This means that the observed differences in ferroxidase reactivity must be explained by the effect of the mutations on other parameters not assessed in this EXAFS study, such as the affinity of each of sites A and B for the metal ion, and the subsequent reactivity towards dioxygen. In spite of the apparent rigidity of the dinuclear site the rHuHF complexes show a variation in reactivity that is reflected in the iron oxidation states and coordination geometries. As in the case of the oxidised DdBfr (C), considerable mineralisation has occurred for the wild type and the most reactive mutant (rHuHF-E27D), resulting in EXAFS-detectable Fe–Fe distances of 3.4 Å.

Acknowledgments We thank Noëlle Carette for the construction of rHuHF-K86Q plasmid, and René de Gelder (Nijmegen) for the model compound search in the CSD. EMBL access for L.T. and M.C.F. was supported by the European Commission, Research Infrastructure Action under Framework Programme 6 "Structuring the European Research Area Specific Programme", contract no. RII3-CT-2004-506008, and for M.G.C. by the EMBL Hamburg Outstation Strategic Fund. Marie Curie and ESRF studentship were provided to M.G.C.

References

1. Crichton RR (2001) Inorganic biochemistry of iron metabolism. Wiley, Chichester
2. Ha Y, Shi D, Small GW, Theil EC, Allewell NM (1999) J Biol Inorg Chem 4:243–256
3. Sun S, Arosio P, Levi S, Chasteen ND (1993) Biochemistry 32:9362–9369
4. Bauminger ER, Harrison PM, Hechel D, Hodson NW, Nowik I, Treffry A, Yewdall SJ (1993) Biochem J 296(Pt 3):709–719
5. Lawson DM, Artymiuk PJ, Yewdall SJ, Smith JM, Livingstone JC, Treffry A, Luzzago A, Levi S, Arosio P, Cesareni G (1991) Nature 349:541–544
6. Hempstead PD, Hudson AJ, Artymiuk PJ, Andrews SC, Banfield MJ, Guest JR, Harrison PM (1994) FEBS Lett 350:258–262
7. Stillman TJ, Hempstead PD, Artymiuk PJ, Andrews SC, Hudson AJ, Treffry A, Guest JR, Harrison PM (2001) J Mol Biol 307:587–603
8. Toussaint L, Bertrand L, Hue L, Crichton RR, Declercq JP (2007) J Mol Biol 365:440–452
9. Macedo S, Romao CV, Mitchell E, Matias PM, Liu MY, Xavier AV, LeGall J, Teixeira M, Lindley P, Carrondo MA (2003) Nat Struct Biol 10:285–290
10. Sayers DE, Theil EC, Rennick FJ (1983) J Biol Chem 258:14076–14079
11. Strange R, Morante S, Stefanini S, Chiancone E, Desideri A (1993) Biochim Biophys Acta 1164:331–334
12. Heath SL, Charnock JM, Garner CD, Powell AK (1996) Chem Eur J 2:634–639
13. Hwang J, Krebs C, Huynh BH, Edmondson DE, Theil EC, Penner-Hahn JE (2003) Science 287:122–125
14. da Costa PN, Romao CV, LeGall J, Xavier AV, Melo E, Teixeira M, Saraiva LM (2001) Molecular microbiology, pp 217–227
15. Ausubel FM, Brent R, Kingston RE, Moore DD, Seidman JG, Smith JA, Struhl K (1995) Current protocols in molecular biology. Greene Publishing Associates/Wiley Interscience, New York
16. Prozzi D, Crichton RR, Davison J (1988) FEBS Lett 234:61–64
17. Shatzman AR, Rosenberg M (1987) Hepatology 7:30S–35S
18. Hermes C, Gilberg E, Koch MHJ (1984) 222:207–214
19. Pettifer RF, Hermes C (1985) J Appl Crystallogr 18:404–412
20. Nolting H-F, Hermes C (1992) EXPROG. EXAFS Data Reduction Package, EMBL Outstation Hamburg, Germany
21. Gurman SJ, Binsted N, Ross I (1986) J Phys C Solid State Phys 19:1845–1861
22. Gurman SJ, Binsted N, Ross I (1984) J Phys C Solid State Phys 17:143–151
23. Rehr JJ, Booth CH, Bridges F, Zabinsky SI (1994) Phys Rev B 49:12347–12350
24. Krebs C, Edmondson DE, Huynh BH (2002) Methods Enzymol 354:436–454
25. Herold S, Lippard SJ (1997) J Am Chem Soc 119:145–156
26. Rohrer JS, Islam QT, Watt GD, Sayers DE, Theil EC (1990) Biochemistry 29:259–264
27. Shulman RG, Eisenberger P, Blumberg WE, Stombaugh NA (1975) Proc Natl Acad Sci USA 72:4003–4007
28. Sayers DE, Stern EA, Herriott JR (1975) J Chem Phys 64:427–428
29. Thorp HH (1992) Inorg Chem 31:1585–1588
30. Carrondo MA, Bento I, Matias PM, Lindley PF (2007) J Biol Inorg Chem 12:429–442
31. Harding MM (2001) Acta Crystallogr D Biol Crystallogr 57:401–411
32. Stenkamp RE, Sieker LC, Jensen LH (1983) Acta Crystallogr B 39:697–703
33. Strange RW, Ellis M, Hasnain SS (2005) Coord Chem Rev 249:197–208
34. Mackle P, Garner CD, Ward RJ, Peters TJ (1991) Biochim Biophys Acta 1115:145–150
35. Mijovilovich A, Meyer-Klaucke W (2003) J Synchrotron Radiat 10:64–68
36. Feiters MC, Eijkelenboom AP, Nolting HF, Krebs B, van den Ent FM, Plasterk RH, Kaptein R, Boelens R (2003) J Synchrotron Radiat 10:86–95
37. Eggers-Borkenstein P, Priggemeyer S, Krebs B, Henkel G, Simonis U, Pettifer RF, Nolting HF, Hermes C (1989) Eur J Biochem 186:667–675
38. Randall CR, Zang Y, True AE, Que L Jr, Charnock JM, Garner CD, Fujishima Y, Schofield CJ, Baldwin JE (1993) Biochemistry 32:6664–6673
39. Kröger M, Folli C, Walter O, Doring M (2006) Adv Synth Catal 348:1908–1918
40. Darensbourg DJ, Wildeson JR, Yarbrough JC (2001) Organometallics 20:4413–4417
41. Yang CY, Meagher A, Huynh BH, Sayers DE, Theil EC (1987) Biochemistry 26:497–503